Air-Sensitivity Study on $LiNiO_2$ Layered Cathode Materials by Using *Ab Initio* Molecular Dynamics Simulations

Xian-Qi Xu,[1,†] Jun-Yan Chen,[1,†] Jia-Hua Liu,[1] Yi-Ning Jia,[1] Chi Fang,[1] Jun-Yu Jiao,[1] Feng Pan,[1] Jia-Xin Zheng,[1,*] Yao Jiang,[2] Bo Xu,[2] and Chu-Ying Ouyang[2]

[1] *School of Advanced Materials, Peking University, Shenzhen Graduate School, Shenzhen, People's Republic of China*

[2] *Fujian Science & Technology Innovation Laboratory for Energy Devices of China (21C-LAB), Ningde, People's Republic of China*

(Received 23 November 2022; revised 12 April 2023; accepted 11 May 2023; published 6 July 2023)

Nickel-rich layered oxides are important cathode materials for lithium batteries, but their effectiveness is compromised by air sensitivity. Using $LiNiO_2$ as a prototype in *ab initio* molecular dynamics simulations, we find that oxygen active sites provide molecular orbitals and metal activation that work in synergy to form impurity hydroxyl and carbonate species in the presence of air. This mechanism successfully explains the high air sensitivity on the specific surfaces, the air-sensitivity transition after Li/Ni mixing, and the treatment effect of cation (Co and Mn) and anion (F and S) doping methods. Doping with sulfur ions proves to have the best protective effect against H_2O and CO_2. A series of first-principles calculations show that oxygen active sites originate from electron loss, and the activation effect of metals is limited by the type of elements, the number of coordination bonds, the coactivation effect and the Jahn-Teller distortion. While impurity formation is usually a localized phenomenon, the autoprotolysis of H_2O allows long-distance proton transport to support the hydrolysis reaction. The adsorption energy of H_2O and CO_2 is not directly related to the air sensitivity, but is inversely proportional to the surface thermodynamic stability in the study of Li/Ni mixing. However, the concentration of Li/Ni mixing depends on the exposed surface, implying that the influence of Li/Ni mixing on air sensitivity and air adsorption capacity is uneven. Our studies contribute to realizing a cost-effective and convenient experimental strategy for treating air sensitivity of $LiNiO_2$ cathode materials.

DOI: 10.1103/PRXEnergy.2.033001

I. INTRODUCTION

In support of the transition to renewable energy, lithium-ion batteries (LIBs) are widely used for energy storage in hybrid and purely electric vehicles. To date, endurance is still one of the main obstacles restricting the promotion of electric vehicles. Ni-rich layered oxides ($LiNi_xM_yO_2$, $x \geq 0.8$, $x + y = 1, M = Co, Mn, Al$) are one of the most promising cathode materials to achieve high energy density (>200 mAh g^{-1}) with low cost and toxicity [1–4]. However, while inheriting the high energy density of $LiNiO_2$, it also inherits many disadvantages such as poor cycle performance, safety performance degradation, and high air sensitivity [2–5]. Air sensitivity is a particularly noteworthy issue because the weak Ni—Ni bonding will lead to the aggregation of Ni ions on the surface of Ni-rich layered cathode materials [6,7], which further enhances air sensitivity. Experimental observations [5] have shown that air sensitivity increases with increasing nickel content, but the role played by Ni ions in impurity formation remains unclear. In most cases, the impurities on the surface of Ni-rich layered cathode materials are harmful and cause additional economic losses in the process of production, storage, and transportation.

Experiments [8,9] show that the impurities mainly consist of hydroxides, $LiHCO_3$, Li_2CO_3, and NiO-like species. The detrimental details of the impurities are summarized as follows: (i) electronic conductivity, Li^+ conductivity, and electrochemically active lithium decreasing [8,10,11]; (ii) accelerated surface degradation, adverse phase transformation, and secondary particle cracking rapidly decrease the capacity retention rate [12]; (iii) local heating with higher impedance increases the risk of catastrophic battery damage and ignition of liquid electrolytes [13–15]; (iv) LiOH and H_2O not only consume electrolytes by electrochemical

*zhengjx@pkusz.edu.cn

†First two authors contributed equally.

reactions but also produce HF, which further corrodes the cathode materials and collectors [11,16–18], and cause the dissolution of transition metals [19–21]; (v) gas evolution [16]; for example, Li_2CO_3 decomposition causes battery bulging and even structural damage; (vi) the high alkalinity initiates defluorination of the polyvinylidene fluoride binder, which leads to the particle agglomeration and slurry gelation [9,22–24]. To combat these hazards, some experimental methods have been developed and proved to be effective, such as cation doping [9,25–27], storage in inert gas [4,8], secondary sintering [8,28], washing and annealing process [29–32], surface coating [33–36], and gradient design [37–40]. Surprisingly, compared with the development of experimental technology, there are few studies on the atomic-scale formation mechanism of impurities [41,42].

From a macroscopic perspective, the surface of Ni-rich cathode materials is considered chemically active in absorbing H_2O and CO_2. Because of the low surface energy, the primary particles are smaller than in the case of low Ni, thus obtaining a larger total surface area for surface chemical reactions [5,43]. In addition, excess lithium is beneficial to suppressing Li/Ni mixing, but introduces additional active lithium oxides Li_2O and Li_2O_2 [44–46] on the surface to react with H_2O and CO_2 to form LiOH and Li_2CO_3 [11,47]. From a microscopic perspective, two chemical reaction mechanisms have been used to explain impurity formation: (1) the redox mechanism [4,8] and (2) the H^+/Li^+ exchange mechanism [4,48–50]. (1) According to crystal field theory, Ni^{3+} with an electron configuration of $t2g^6eg^1$ tends to induce the Jahn-Teller distortion in an octahedral coordination environment. Therefore, Ni^{3+} on the surface tends to turn into Ni^{2+} with an electron configuration of $t2g^6eg^2$ to prevent lattice distortions. However, the reduction of Ni^{3+} to Ni^{2+} also results in the formation of oxygen active sites on the surface, which react with H_2O, CO_2, and Li^+ to form LiOH, $LiHCO_3$, and Li_2CO_3. At the same time, due to the consumption of lithium and oxygen, a NiO-like thin layer is formed between the adsorption layer and the bulk material. The redox mechanism is as follows:

$$2Ni^{3+} + 2O_s^{2-} \rightarrow 2Ni^{2+} + O_{s,\text{active}}^{2-} + \tfrac{1}{2}O_2, \quad (1a)$$

$$O_{s,\text{active}}^{2-} + CO_2 \rightarrow CO_3^{2-}, \quad (1b)$$

$$O_{s,\text{active}}^{2-} + H_2O \rightarrow 2OH^-, \quad (1c)$$

with subscript s indicating that O^{2-} is the lattice oxygen on the $LiNiO_2$ surface. (2) Li^+ migrate outward and protons diffuse into the bulk phase. Shkrob *et al.* [49] proposed that the interaction of H^+ with lattice oxygen is responsible for the c-axis contraction when $LiNi_{0.5}Co_{0.2}Mn_{0.3}O_2$ is exposed to humid air. The H^+/Li^+ exchange mechanism is as follows:

$$Li^+ + H_2O \rightarrow H^+ + LiOH, \quad (2a)$$

$$LiOH + CO_2 \rightarrow LiHCO_3, \quad (2b)$$

$$LiOH + LiHCO_3 \rightarrow H_2O + Li_2CO_3, \quad (2c)$$

$$2NiOOH \rightarrow 2NiO + H_2O + \tfrac{1}{2}O_2. \quad (2d)$$

Although some experimental results support the H^+/Li^+ exchange mechanism, the promotion effect of high nickel content on impurity formation cannot be explained. Therefore, the H^+/Li^+ exchange mechanism is thought to usually occur in the primary stage of air exposure [4].

Interestingly, some experiments show that Li_2CO_3 is formed on the surface of Ni-rich cathode materials in pure CO_2 [51–53], while others show that H_2O is necessary for chemical reactions [54]. This obvious contradiction may be attributed to the fact that the residual lithium oxides are not excluded or the difference in synthesis methods leads to the exposure of different surfaces. To solve the above contradiction and study the details of the impurity formation in air, we employ *ab initio* molecular dynamics (AIMD) simulations to study the air sensitivity of the (003), (012), (101), (100), (104), and (110) surfaces of $LiNiO_2$ in pure H_2O and CO_2 atmosphere, and ignore the residual lithium oxides on the surface in this work. It should be emphasized that, since high nickel content accelerates the formation of impurities, we target $LiNiO_2$ to study instead of $LiNi_xM_yO_2$ ($M = Co, Mn, Al$). The chemical activity of surface oxygen ions and the activation ability of metal ions are analysed through a series of first-principles calculations (the structural relaxation, density of states, spin electron density, partial density of states, and crystal orbital Hamilton population calculations) to explain the air sensitivity of the $LiNiO_2$ surface. Furthermore, we also study the contribution of Li/Ni mixing to air sensitivity. Finally, we study and discuss the protective effect of cation and anion doping on the $LiNiO_2$ surface.

II. RESULTS AND DISCUSSION

A. Air sensitivity on six surfaces

The AIMD simulations are performed to simulate different surfaces of $LiNiO_2$ in pure H_2O (1 ps) and CO_2 (2 ps). The reason for using different AIMD simulation durations is that the number of CO_2 molecules is only half the number of H_2O molecules when the densities of the two are set close to each other (1.0 g/cm^3 for H_2O and 1.1 g/cm^3 for CO_2), which means that the probability of CO_2 contacting the surface is only half that of H_2O. As shown in Figs. 1(a)–1(f), hydrolysis reactions (separation of H^+ and OH^-) can be observed within 1 ps on the (003), (100) and (110) surfaces but not on the (104), (101) and (012) surfaces, suggesting that the latter are more inert.

The structural relaxation calculations (SRCs) further verify the results of AIMD simulations (Fig. S6 within the Supplemental Material [55]) and are used to observe the whole process of the hydrolysis reaction. As an example, the (100) surface is selected to describe the detail of this process in Fig. S7(a) within the Supplemental Material [55]. When the hydrolysis reaction is desired, H_2O is first adsorbed on one Ni ion. Then H^+ is transferred to active O_s^{2-} on the $LiNiO_2$ surface and OH^- formed by hydrolysis tends to occupy the vacancies of metal octahedron coordination. By performing partial density-of-states calculations, Ni^{2+} and Ni^{4+} are found on the (003), (100), and (110) surfaces [Fig. S8(a) within the Supplemental Material [55]]. The presence of Ni^{2+} on the surface of $LiNiO_2$ has been confirmed by Liu *et al.* [8] and Zheng *et al.* [32] from x-ray photoelectron spectroscopy analysis. However, the presence of Ni^{4+} on the surface has rarely been mentioned so far. Our view is that the presence of Ni^{4+} is beneficial to avoid the production of O^- and thus reduces the energy of the system in the initial stage of impurity formation. According to the redox mechanism, the reduction of Ni^{3+} to Ni^{2+} can activate O_s^{2-} on the surface. The evidence of the presence of active O_s^{2-} will be exhibited later. As shown in Fig. S8(b) within the Supplemental Material [55], only Ni^{3+} is found on the (104), (101), and (012) surfaces, so O^{2-} on these surfaces may be inactive. The details of judging the valence state of Ni ions are shown in Sec. S7 within the Supplemental Material [55]. Here, we propose the formation mechanism of active oxygen sites and hydrolysis reaction process as follows:

$$O_s^{2-} + 2Ni^{3+} \rightarrow Ni^{2+} + Ni^{4+} + O_{s,\text{active}}^{2-}, \tag{3}$$

$$\begin{aligned} &Li^+ + O_{s,\text{active}}^{2-} + H_2O \rightarrow LiOH + OH^-, \\ &Ni^{2+} + O_{s,\text{active}}^{2-} + H_2O \rightarrow NiOH^+ + OH^-, \end{aligned} \tag{4}$$

where subscript s indicates that the O^{2-} is the lattice oxygen on the $LiNiO_2$ surface. Equation (3) is used to explain the production of oxygen active sites $O_{s,\text{active}}^{2-}$ rather than to indicate that we observe the disproportionation process on the surface. In Eq. (4), based on our observations from AIMD simulations, the $O_{s,\text{active}}^{2-}$ provide the molecular orbital to accept H of H_2O, while the metal as the activator weakens the O—H bond within H_2O, thereby reducing the energy barrier of the hydrolysis reaction. We prove this conjecture in the subsequent discussion. Eom *et al.* [25] experimentally proved that increasing the content of Co can effectively inhibit the formation of impurities, which indicates that metal is also a crucial factor to participate in the chemical reaction on the surface of cathode materials. In order to visually demonstrate the role of metals in hydrolysis, we calculate the bond length and strength of H_2O in vacuum and on surfaces. Table S2 within the Supplemental Material [55] shows that the bond strengths of O—H bonds on the (012), (101), and (104) surfaces (−4.4 to −3.9 eV) are weaker than that in vacuum (−7.4 eV), which indicates that metal ions contribute to weakening the binding of O and H within H_2O. In addition, we find that the formation of hydrogen bonds between the H atom and surface oxygen O_s^{2-} lengthens the O—H bond (0.97 to 1.00 Å) and weakens the bond strength. This attractive interaction will further help H atoms escape from H_2O. We also attempted to delete Ni ions on the (100) surface and Li ions on the (003) surface to observe whether or not the hydrolysis reaction still occurred in SRCs. The results [Fig. S7(c) within the Supplemental Material [55]] prove that metal weakening the O—H bond is a non-negligible reaction stage for the hydrolysis reaction. Therefore, at least in the primary stage of impurity generation, the microdynamics process of the hydrolysis reaction should be a combination of the H^+/Li^+ and redox mechanisms because Eqs. (1) ignore the activation of metals and Eqs. (2) lack active oxygen. An additional reaction process, the autoprotolysis phenomenon [56], is observed to promote the hydrolysis reaction. In order to explain this phenomenon more clearly, SRCs are performed to reproduce the results of AIMD simulations. As shown in Figs. 1(g)–1(i), when an additional water molecule is added, No. 1 H_2O transferred protons to No. 2 H_2O to complete the hydrolysis reaction. Then, No. 2 H_2O transferred protons to $O_{s,\text{active}}^{2-}$. The protons transfer mechanism is as follows:

$$\begin{aligned} &Li^+ + 2H_2O \rightarrow LiOH + H_3O^+ \\ &Ni^{2+} + 2H_2O \rightarrow NiOH^+ + H_3O^+ \end{aligned} \tag{5}$$

$$H_3O^+ + O_{s,\text{active}}^{2-} \rightarrow +H_2O + OH^- \tag{6}$$

With the help of the abundant hydrogen bond network, excess water molecules not only do not hinder the hydrolysis reaction, but may also be beneficial to the proton transport over long distances when metals and oxygen active sites are far apart. We predict that the autoprotolysis phenomenon will accelerate the formation of impurities under high humidity conditions.

The air sensitivity of the $LiNiO_2$ surfaces to pure CO_2 is similar to that of pure H_2O in AIMD simulations [Figs. 1(j)–1(o)] and SRCs (Fig. S6 within the Supplemental Material [55]). The significant changes in the O—C—O bond angle (180° to approximately 120°) are observed on the (003), (100), and (110) surfaces, which means that the hybridization mode of CO_2 has changed (sp to sp^2). By further observing each frame of the reaction process, the formation of CO_3^{2-} is found to take place under the activation of metals, not between CO_2 and $O_{s,\text{active}}^{2-}$ [Fig. S7(b) within the Supplemental Material [55]]. Once the metal ions at the reaction site are deleted, the conversion of CO_2 to CO_3^{2-} is not found in SRCs [Fig. S7(d) within the Supplemental Material [55]]. In Table S2 within the Supplemental Material [55], the weakening of the O—C bond strength from vacuum (−18.4 eV) to surface

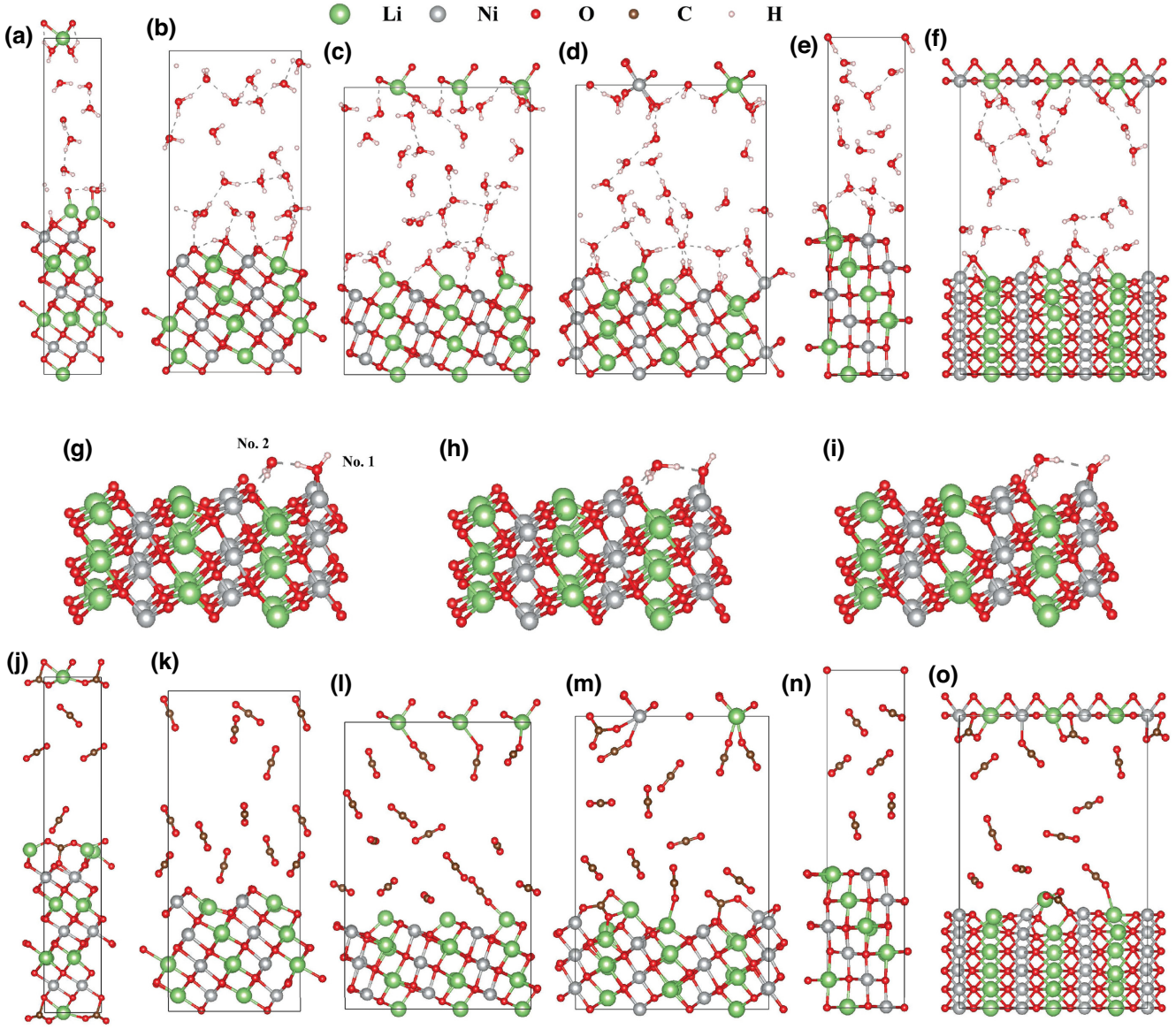

FIG. 1. AIMD snapshots of (003), (012), (101), (100), (104), and (110) in pure H_2O after 1 ps (a)–(f) and pure CO_2 after 2 ps (j)–(o). (g)–(i) Three stages of the autoprotolysis phenomenon on the (100) surface by SRCs. The green, silver, red, brown, and white ball models represent the elements Li, Ni, O, C, and H, which are applicable to the whole article. All AIMD trajectories can be found in the Video within the Supplemental Material [55].

(−10.1 to −9.4 eV) also implies that the metals can activate electron rearrangement to form an active CO_2. These observations show the importance of the joint participation of metals and oxygen active sites once again. The formation mechanism of CO_3^{2-} is as follows:

$$\begin{aligned} Li^+ + O^{2-}_{s,\text{active}} + CO_2 &\rightarrow LiCO_3^- \\ Ni^{2+} + O^{2-}_{s,\text{active}} + CO_2 &\rightarrow NiCO_3 \end{aligned} \tag{7}$$

Combining with the results of AIMD simulations in pure H_2O and CO_2, we define the (100), (110), and (003) surfaces as highly air-sensitive surfaces as well as the (012), (101), and (104) surfaces as lowly air-sensitive surfaces. The reaction is spontaneous on the former, but needs to cross the reaction barrier on the latter. The reaction energy barrier calculations show that the hydrolysis reaction is difficult to perform on the (104) surface (0.88 eV), but relatively easy on the (101) and (012) surfaces (0.13 eV). The adsorption energy [see Eq. (8) below for a definition] obtained by SRCs shows that (Table I) there is no direct positive correlation between air sensitivity and adsorption capacity. The adsorption energy mainly comes from the formation of coordination bonds between O atoms of H_2O and CO_2 and metal ions to reduce the surface energy. Higher adsorption energy indicates stronger coordination

TABLE I. The adsorption energy on different surfaces in pure H_2O and CO_2.

	003	012	101	110	104	100
H_2O (eV)	−0.81	−1.00	−0.88	−1.66	−0.61	−3.06
CO_2 (eV)	−0.71	−0.43	−0.39	−1.54	−0.39	−1.54

bonds, which may weaken the O—H and C—O bonds to a greater extent. However, this is not the only condition for chemical reactions. Oxygen active sites also play an important role in the reaction process. For highly air-sensitive surfaces, the exothermic chemical reaction also contributes part of the adsorption energy.

In order to explain the high air sensitivity on the (003), (100), and (110) surfaces, density of states (DOS) and spin electron density calculations are performed for Li, Ni, and O ions on the $LiNiO_2$ surfaces. As shown in Fig. 2(a), the electron energy of O_s^{2-} on the (003), (100), (110) surfaces is closer to or even reaches the Fermi energy, which proves that the O_s^{2-} are indeed activated by the reduction of Ni^{3+} to Ni^{2+} . However, we also observe that O_s^{2-} of the (012) surface is active, but does not arise from the valence change of transition metals. Therefore, the presence of Ni^{2+} is not a unique mechanism for the production of active O_s^{2-}. The absence of coordination bonds may also achieve a similar effect. Because of the loss of electrons,

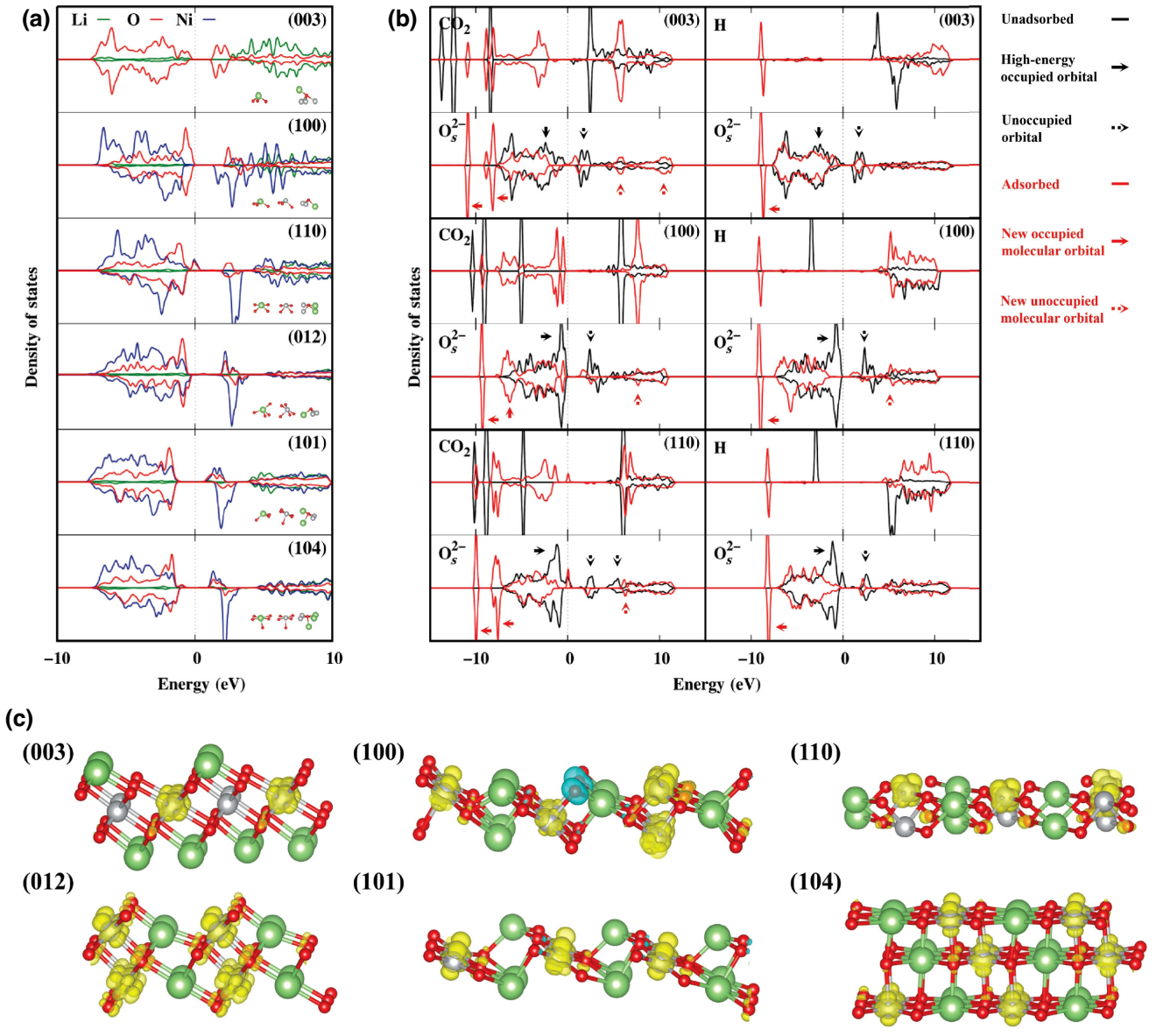

FIG. 2. (a) DOS of Li, Ni, and O ions for six kinds of surface. (b) DOS of air molecules and O_s^{2-} before and after adsorption on the (003), (100), and (110) surfaces. (c) Spin electron density maps for six kinds of surface. Yellow means spin up and blue means spin down.

O_s^{2-} becomes more active and its electrons are pushed to higher energy levels. These high-energy occupied orbitals and partially empty orbitals near the Fermi energy tend to combine with H of H_2O and C of CO_2 to form new molecular orbitals [Fig. 2(b)]. On the other hand, although the DOS of Li and Ni ions show no significant difference between the highly air-sensitive and the lowly air-sensitive surfaces, we note that the number of missing coordination bonds of metal ions on the surfaces may affect the activation effect. In Fig. 2(c), the spin electron density (unpaired electrons) is mainly concentrated in the direction of coordination bonds. Therefore, the Ni ions on the (100) surface have the largest bonding space and strongest bonding ability because they lost the most coordination bonds. In other words, the Ni ions on the (100) surface have the strongest activation. We think that same conclusion holds for Li ions as Ni ions, although we cannot see the spin electron density of Li ions. In addition, the coactivation of metal ions is also considered to strengthen the catalysis further. For example, the O atom of H_2O bonding with two metal ions on the (003), (100), and (110) surfaces is observed after the hydrolysis reaction [Figs. S6(a), S6(b), and S6(f) within the Supplemental Material [55]]. Generally, the activation of the Li ion is weaker than that of the Ni ion, so there is a more urgent need for coactivation on the (003) surface to weaken the C—O and O—H bonds. As shown in Fig. S7(e) within the Supplemental Material [55], the inability of one single Li ion to achieve a hydrolysis reaction is proved by SRCs. In general, the coactivation depends on the spatial positions of Li and Ni ions and the direction of missing coordination bonds that are limited to the exposed surface, but Li/Ni mixing and metal ion migration may change the original surface morphology and affect the local chemical activity of the surfaces. Another possibility to influence the activation capacity of the metal is the Jahn-Teller distortion. According to crystal field theory, the Jahn-Teller distortion is easily induced by Ni^{3+} on the surface [Fig. 3(a)]. This distortion leads to two results.

1. Because of the repulsion of d_{z^2} orbital electrons, the distance between the air molecule and the surface of $LiNiO_2$ is increased compared to the case without the Jahn-Teller distortion [Fig. 3(b)], which causes a mismatch with the lattice site and thus weakens the metal activation.
2. Additional energy is required in the reaction to drive the transfer in the distortion direction, i.e., the electron renormalization within Ni^{3+} [Fig. 3(c)].

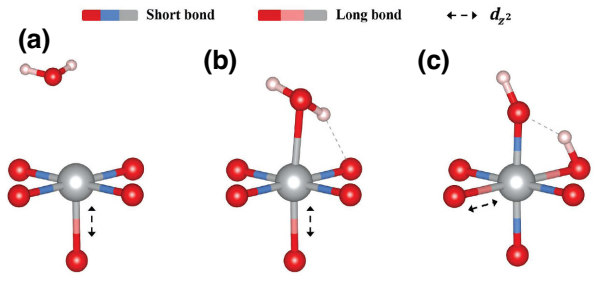

FIG. 3. Coordination models for Ni^{3+} on lowly air-sensitive surfaces including before adsorption (a), after adsorption (b), and after hydrolysis (c).

Both make it more difficult for chemical reactions to take place on the lowly air-sensitive surfaces. A detailed discussion can be found in Sec. S12 within the Supplemental Material [55]. In a word, the high activity of oxygen ions and metal activation form a synergistic effect to achieve a highly air-sensitive surface.

B. Li/Ni mixing on air sensitivity

Li/Ni mixing is the most common and the largest number of defects in $LiNiO_2$ layered materials, so its impact on air sensitivity should also be considered. The (012), (101), and (104) surfaces with low air sensitivity are selected to exchange the positions of Li and Ni ions. Previous work [57] shows that Li ions are more exposed than Ni ions, so we just consider two exchange modes, including Li-exposed to the outermost layer (Li-exposed mode) and Li-Ni exchanged in the same layer (same layer mode), as shown in Fig. S3 within the Supplemental Material [55]. Since the effect of Li/Ni mixing on air sensitivity is usually localized at the ionic exchange, we choose SRCs to study rather than AIMD simulations in this part.

By calculating the formation energy of Li/Ni mixing [see Eq. (9) below for a definition] on the (012), (101), and (104) surfaces, the Li-exposed mode is found to be more easily formed than the same layer mode [Fig. 4(a)]. Moreover, the priority order of Li/Ni mixing is inconsistent for different surfaces. The formation energy of Li/Ni mixing is almost twice as high on the (012) and (101) surfaces than on the (104) surface, which means that Li/Ni mixing is more difficult to perform on the former two surfaces, but occurs readily on the latter. We predict that the (104) surface has a higher concentration of Li/Ni mixing than the other two surfaces.

The influence of Li/Ni mixing on the air adsorption capacity and air sensitivity is also studied by SRCs, as shown in Figs. 4(c)–4(l). Note that CO_2 adsorbed on the (012) surface of the Li-exposed mode produced an additional O—O dimer [Fig. 4(j)], resulting in overestimating the adsorption energy. Therefore, the adsorption energy of the overestimation system is excluded. Equations (9)–(11) prove that the difference in surface energy is directly related to the Li/Ni mixing formation energy. This difference is used to determine which surface is thermodynamically more stable. As shown in Fig. 4(a), the difference in surface energy is inversely proportional to the adsorption energies of H_2O and CO_2 on the same

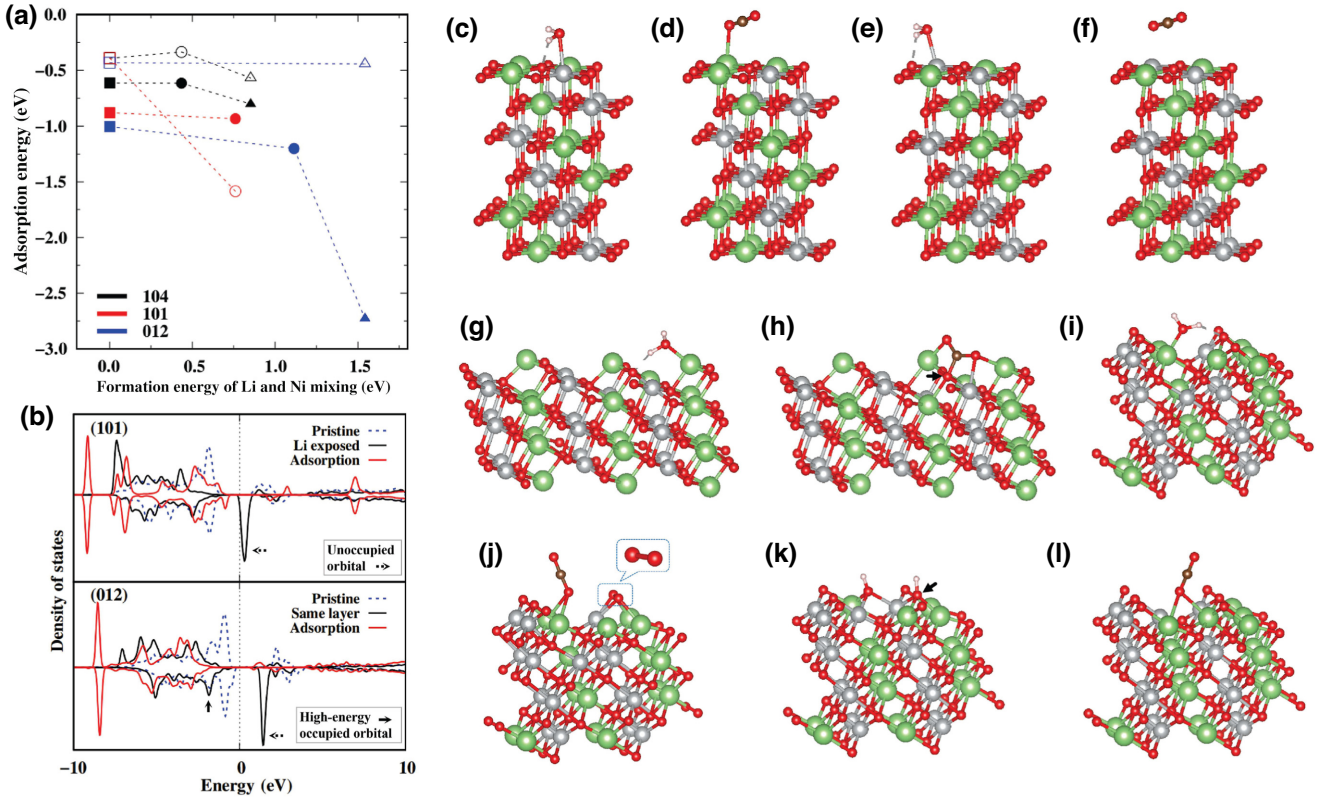

FIG. 4. (a) The formation energy of Li/Ni mixing versus the adsorption energy of H_2O (filled symbols) and CO_2 (open symbols). Here a square denotes the pristine state, a circle denotes the Li-exposed mode, and a triangle denotes the same layer mode. Dashed lines are used to aid in observing results. (b) The DOS of O_s^{2-} in the (101) and (012) surfaces include the pristine state, Li/Ni mixing, and the adsorption model. (c),(d) The Li-exposed mode and (e),(f) the same layer mode on the (104) surface. (g),(h) The Li-exposed mode on the (101) surface. (i),(j) The Li-exposed mode on the (012) surface. (k),(l) The same layer mode on the (012) surface. The black arrow points to O_s^{2-} at the reaction site.

crystallographic surface, except in a few cases. This implies that the adsorption energy may be directly related to the thermodynamic stability of the $LiNiO_2$ surface. Thermodynamically unstable surfaces have greater adsorption capacity for H_2O and CO_2. The reason for this result may be that thermodynamically unstable surfaces prefer to adsorb air molecules to reduce the surface energy. Since thermodynamic stability is not a direct condition for chemical reactions, our conclusions may not apply to systems with air-sensitivity transition.

More interestingly, on the (101) surface of the Li-exposed mode and the (012) surface of the same layer mode, the transition from the lowly air-sensitive surface to the highly air-sensitive surface is observed under the Li/Ni mixing effect [Figs. 4(h) and 4(k)]. As shown in Fig. 4(b), the DOS of O_s^{2-} before and after adsorption at the reaction site are calculated to explain this transition. Compared with the pristine state, O_s^{2-} on the (101) and (012) surfaces before adsorption have more empty orbitals near the Fermi energy. The presence of these empty orbitals indicates that the electrons of O_s^{2-} are unsaturated, and their disappearance after adsorption indicates that they are directly involved in chemical reactions. Through PDOS calculation (Fig. S9 within the Supplemental Material [55]), we find that Li/Ni mixing will lead to the disproportionation of Ni^{3+} and the reduction of Ni^{3+} to Ni^{2+}, but these are not the main reasons for the generation of empty orbitals of O_s^{2-} because they do not occur near the reaction site. A more direct reason is that the Ni^{3+} at the reaction site is replaced by Li^+, resulting in the electron loss of the O_s^{2-}. In addition, coactivation also contributes to the hydrolysis reaction and the formation of CO_3^{2-}. As shown in Figs. 4(h) and 4(k), O atoms of H_2O and CO_2 are observed to bond with three metal ions to form a strong coactivation effect. In these two systems, we do not find the transfer in the Jahn-Teller distortion direction (see Sec. S12 within the Supplemental Material [55] for details). Based on these analyses, we believe that the reasons for the air-sensitivity transition are consistent with the previous section (high air sensitivity on the surfaces). Meanwhile, the air-sensitivity transition also confirms that the formation of impurities can be inhibited by controlling the activity of O_s^{2-} and the activation ability of metals.

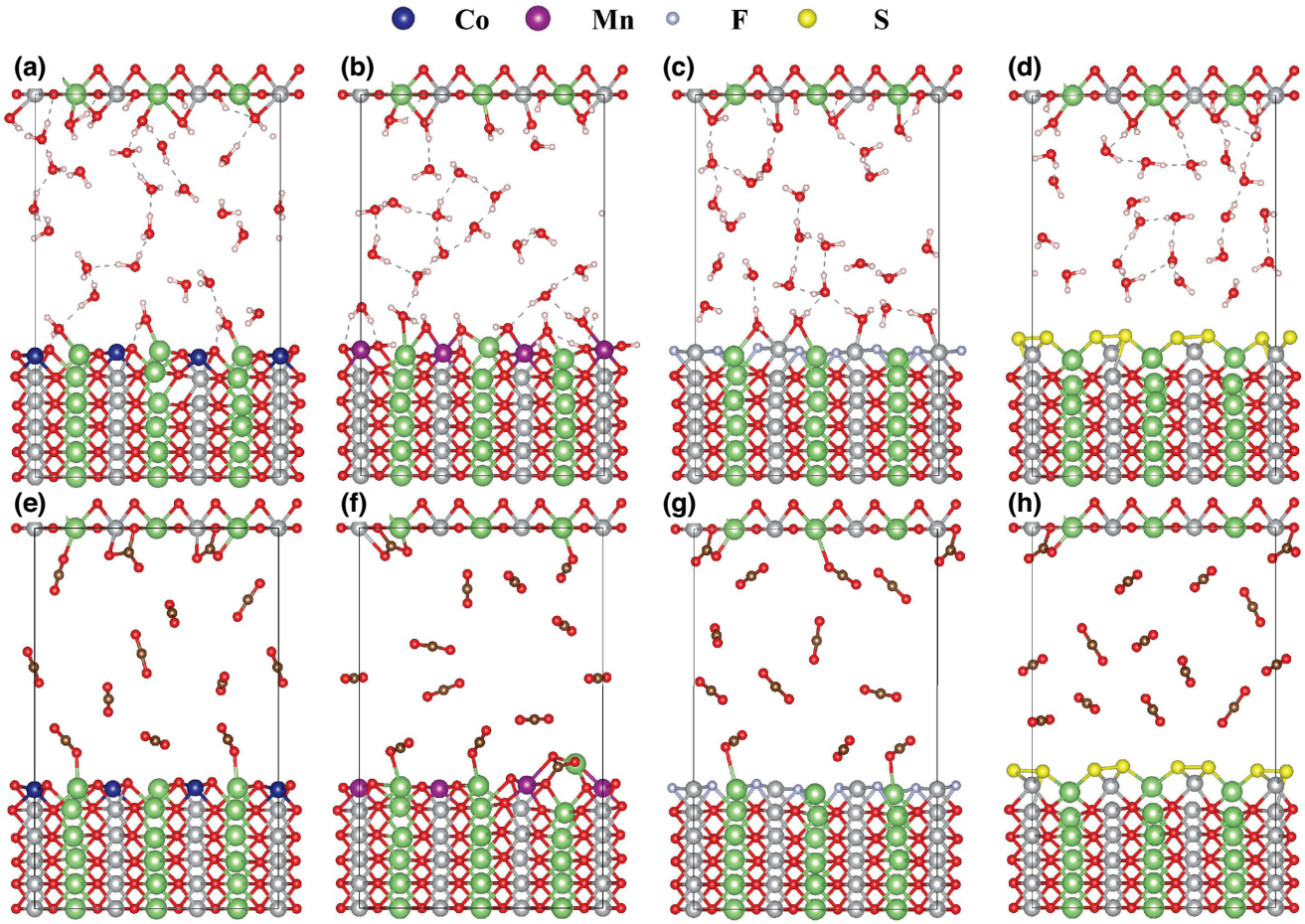

FIG. 5. Doping Co, Mn, F, S on the (110) surfaces in pure H_2O (a)–(d) and pure CO_2 (e)–(h).

C. Cation and anion doping effect on air sensitivity

We find that both metals and oxygen active sites play important roles in chemical reactions on the $LiNiO_2$ surface. Therefore, we attempted cation doping (Co or Mn instead of Ni) and anion doping (F or S instead of O) to treat air sensitivity, respectively. Elements Co and Mn are very common in ternary layered cathode materials. Elements F [58] and S [59] have also been shown to be doped into Ni-rich layered materials. The (110) surface is selected as the research object because it has a higher density of active sites than others. In order to check whether the doped elements appear on the surface, we perform formation energy calculations [see Eq. (12) below] for substitution doping at low doping concentrations (one Ni or O is replaced, as shown in Fig. S4 within the Supplemental Material [55]). The formation energies of the substitutional doping are −2.0, −3.7, −2.3, and 1.3 eV for Co, Mn, F, and S, respectively. The formation energy of F lies within the range between those of Co and Mn, indicating that F atoms can easily occur on this surface. The formation energy of the S atom is positive, indicating that S atoms are more difficult to be doped into the surface than F atoms. In order to observe the effect of doping elements on air sensitivity from AIMD simulations more conveniently, we construct ideal surface models with high doping concentration, as shown in Fig. S5 within the Supplemental Material [55]. As far as current experimental techniques are concerned, these ideal surface models cannot be applied in real situations yet, but they do not change the qualitative results on the effect of doped elements on air sensitivity. For all these surface models, we perform AIMD simulations for 5 ps with the *NVT* ensemble to check their stability. Finally, we perform AIMD simulations for 1 ps in pure H_2O and 2 ps in pure CO_2. SRCs are applied to verify the results of the AIMD simulations, as shown in Fig. S10 within the Supplemental Material [55].

As shown in Figs. 5(a), 5(b), 5(e), and 5(f), the chemical reactions are obviously inhibited on the Co-doped surface but still occur on the Mn-doped surface. Compared with their initial surface configurations [Fig. S5(a) within the Supplemental Material [55]], O_s^{2-} with three coordination bonds and four coordination bonds (O_{3b} and O_{4b}) are observed on the Co-doped surface to form an

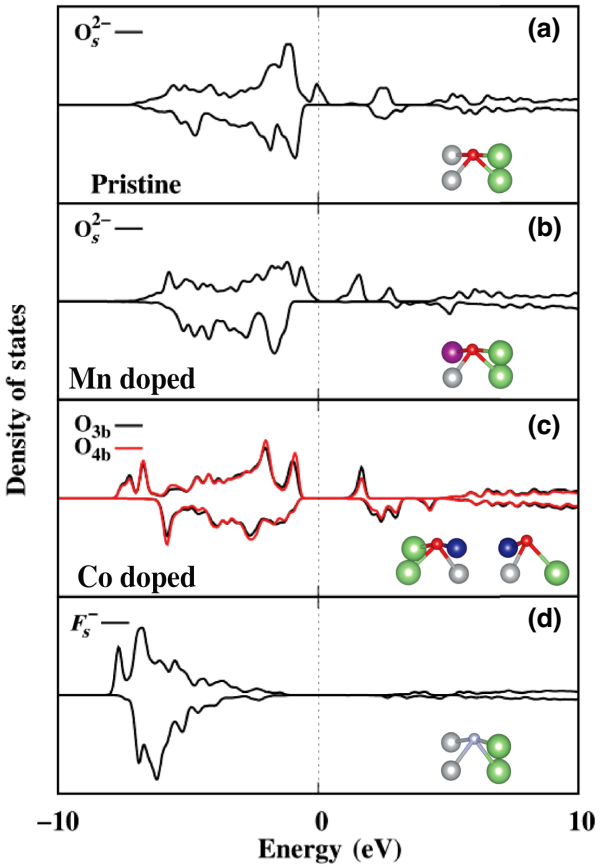

FIG. 6. The DOS of anions on the (110) surfaces with (a) pristine structure, (b) Mn doping, (c) Co doping, and (d) F doping.

uneven morphology different from the Mn-doped surface. This uneven morphology prevents the O atoms of H_2O and CO_2 from bonding with two metal ions to achieve a coactivation effect. To demonstrate the effect of transition metals on the activity of oxygen ions, we calculate the lengths and strengths of the M—O bond (M = Ni, Mn and Co) on the surface. The bond lengths of Co-O_{3b}, Co-O_{4b}, Mn-O, and Ni-O are 1.70, 1.73, 1.86, and 1.98 Å, respectively, and the bond strengths (spin up/spin down) are $-2.7/-3.8$, $-2.4/-3.3$, $-2.3/-2.6$, and $-1.6/-1.8$ eV, respectively. Obviously, the bond strengths of Co-O and Mn-O are stronger than that of Ni-O (Co-O > Mn-O > Ni-O). The strong combination between transition metals and O_s^{2-} is conducive to weakening the activity of O_s^{2-} and hindering electron rearrangement. The DOS of O_s^{2-} is also calculated to support this conclusion. As shown in Figs. 6(a)–6(c), the electron energies of O_s^{2-} on the Co-doped and Mn-doped surfaces are pushed away from the Fermi energy. The order of the activity of O_s^{2-} reflected by the DOS diagram is consistent with the results of bond strength. The PDOS calculations also prove that the O_s^{2-} cannot be activated by reducing the valence state of the doping transition metal (Fig. S11 within the Supplemental Material [55]). Based on the above results, the weakening of metal activation ability and the activity of O_s^{2-} are the main reasons to inhibit the formation of impurities in cation-doped systems.

TABLE II. The adsorption energies on the Co-, Mn-, F-, and S-doped surfaces in pure H_2O and CO_2.

	Co	Mn	F	S
H_2O (eV)	−0.93	−2.08	−1.03	−0.22
CO_2 (eV)	−0.48	−1.89	−0.48	−0.16

As shown in Figs. 5(c), 5(d), 5(g), and 5(h), there are no chemical reactions on the F-doped and S-doped surfaces in pure H_2O and CO_2. Although the electronegativity of F is greater than that of O, which may lead to stronger hydrogen bond attraction, it is difficult for the F ion to provide the molecular orbital to accept H of H_2O and C of CO_2. As shown in Fig. 6(d), the 2*p* orbital of the F ion has been completely occupied when the F-doped surface is in vacuum. In addition, we observe that H_2O and CO_2 can hardly be adsorbed on the S-doped surface. As shown in Table II, the adsorption energy calculations are performed to prove the weakest attractive interaction between the S-doped surface and the air (H_2O and CO_2) compared with other systems. The possible reasons are as follows.

(a) The low electronegativity of S causes a weak hydrogen bond.
(b) S ions wrap the metal ions inside to isolate the interaction between the metal and air.
(c) The outward movement of S ions destroys the crystal potential field on the surface.

Because of the inaccessibility of air to the surface, metal activation is ineffective on the S-doped surface so that the surface chemical reactions cannot occur.

To sum up, we suggest using anion doping to treat air sensitivity of $LiNiO_2$, especially doping S, because S ions not only suppress the formation of impurities, but also prevent H_2O and CO_2 from being brought into the Li-ion battery to cause side reactions.

III. CONCLUSION

The whole process of chemical reaction on $LiNiO_2$ surfaces in pure H_2O and CO_2 was observed in AIMD simulations. Unlike the redox mechanism and H^+/Li^+ exchange mechanism, both oxygen active sites and metal ions were observed to participate in chemical reactions. Based on our observations and analysis, oxygen active sites provide molecular orbitals to bond with H or C atoms, and metal ions are responsible for weakening O—H and

C—O bonds and activating electron rearrangements. By analyzing the results of the spin electron density and SRCs, we concluded that the activation capacity of metal ions is closely related to the type of elements, the number of coordination bonds, the coactivation effect, and the Jahn-Teller distortion. By performing DOS and PDOS calculations, the existence of oxygen active sites was proved to arise from the presence of Ni^{2+}, the absence of coordination bonds, and Li-Ni exchange. But other possibilities to generate oxygen active sites are not ruled out. To sum up the above, we recommend more exposure to Ni^{3+} on the surface to mitigate air sensitivity.

Because of the autoprotolysis phenomenon of H_2O, the formation of impurities may be accelerated in a wet environment. Thus, controlling the concentration of water in the air properly may mitigate the formation of impurities.

Li/Ni mixing can affect the air sensitivity and air adsorption capacity of $LiNiO_2$ surfaces. The activation of O_s^{2-} and the enhancement of metal activation are the main reasons for air sensitivity. The adsorption capacity of $LiNiO_2$ surfaces is not directly related to air sensitivity, but the thermodynamically more unstable surfaces are found to have stronger adsorption capacity for H_2O and CO_2. However, the priority order of Li/Ni mixing is not consistent for different surfaces. We predict that Li/Ni mixing and its influence on air sensitivity and adsorption are likely to be uneven on $LiNiO_2$ surfaces.

Doping Co and Mn can enhance the interaction between the transition metals and the O_s^{2-} to weaken the activity of the O_s^{2-}, but they have only limited support to prevent the O_s^{2-} from reacting with H_2O and CO_2. This is because Co and Mn ions have a certain activation capacity and actually have complex valence states in Ni-rich layered oxides. Anion doping (F, S) is more direct and effective than cation doping (Co, Mn) to treat air sensitivity. Because of the lack of oxygen active sites on the surface of cathode materials, the chemical reactions were completely inhibited in our study. Doping with S is especially recommended since inhibition of interactions with H_2O and CO_2 prevents side reactions in LIBs, but other properties still need to be studied.

With the aid of AIMD simulations, it was also observed on the $LiNiO_2$ surface that Li ions were relocated a short distance from their original lattice by air molecules (H_2O or CO_2) [Figs. 1(a), 1(d), 1(n), and 1(o)]. However, it is almost impossible to explain Li ions migrating to the surface, degradation, and phase transition of the surfaces in the air using short-timescale simulations. We speculate that H ions bound to oxygen active sites will diffuse into the bulk as Li ions continue to migrate to the surface. In the future, observing the dynamic reaction processes on $LiNiO_2$ surfaces over a longer time scale will be interesting and meaningful.

IV. METHODS

Density functional theory calculation are performed using the Vienna *ab initio* simulation package (VASP) [60,61] with the projector-augmented-wave method [62] and the plane-wave basis sets. The plane wave energy cutoff is set to 580 eV. The convergence criteria for the self-consistent field and maximum force are set to 10^{-5} eV and 0.02 eV/Å, respectively. For the AIMD and structural relaxation calculations, the exchange-correlation energy is described by the Perderw, Burke, and Ernzerhof (PBE) functional [63], including the D3 (the Grimme method [64]) dispersion correction. The *NVT* simulations are set to 300 K with the Nosé-Hoover thermostat with timestep = 1 fs. The Hubbard corrected PBE+U functional [65] is applied to correct the strong on-site Coulomb interaction of localized 3*d* electrons on the transition metals. According to previous work, the *U* values are set to 6.2 [66], 3.3 [67], and 3.5 [68] eV for Ni, Co, and Mn, respectively. The DOS and PDOS calculations are performed with the Heyd-Scuseria-Ernzerhof (HSE06) hybrid exchange correlation functional [69], including the D3 dispersion correction using PWmat [70]. The chemical reaction energy barrier is calculated using the Dimer method [71–74].

Bond length and bond strength results are obtained from crystal orbital Hamilton population calculations using the local-orbital basis suite towards electronic-structure reconstruction (LOBSTER) program [75–80]. Images of all the surface models are made using visualization for electronic and structural analysis (VESTA) [81]. The open visualization tool is applied to observe the trajectory of AIMD simulations [82].

The surface models are built based on an α-$NaFeO_2$ layered structure with a $R\bar{3}m$ space group [83,84]. Three nonpolar surfaces, (104), (100), and (110), and three polar surfaces, (003), (012), and (101), are selected to study air sensitivity [57,66]. Although previous theoretical calculations and experiments [57,85,86] have shown that (003) and (104) surfaces are the most stable, it cannot be ruled out that the air erosion starts from some secondary surfaces, and some advanced experimental techniques allow specific surfaces to be exposed to the air as the primary surface [87–90]. To model $LiNiO_2$-H_2O/CO_2 interfaces, we first introduce a vacuum space of 15 Å between slabs. For polar interfaces, we expose the same ions in the two outermost layers (upper and lower surfaces) to eliminate the built-in electric field, and delete one-half of the outermost layers to ensure the stoichiometric ratio. Which atoms are deleted can be found in the Build Model section of the Supplemental Material [55]. The outermost two layers of the lower surface are fixed to weaken the interaction between the two surfaces. Next, we fill the vacuum layer with pure H_2O and CO_2, respectively. But, for calculating adsorption energy, only one H_2O or CO_2 is placed on the $LiNiO_2$

surface. More details are given in the Supplemental Material [55].

The electronic adsorption energy (ΔE_{ads}) is calculated using

$$\Delta E_{ads} = E_{total} - E_{slab} - E_{adsorbate}, \quad (8)$$

where E_{total} and E_{slab} are the total electronic energies of the surface with and without adsorbate adsorbed, and $E_{adsorbate}$ is the total electronic energy of single adsorbate.

The formation energy of Li/Ni mixing ($\Delta E_{formation}$) on the surface is calculated using

$$\Delta E_{formation} = \frac{E_{slab}^{Li/Ni} - E_{slab}}{2}, \quad (9)$$

where $E_{slab}^{Li/Ni}$ is the total electronic energy of the surface after Li/Ni mixing.

The surface energy is defined as

$$\gamma = \frac{E_{slab} - E_{bulk}}{2}, \quad (10)$$

where E_{bulk} is the total electronic energy of the bulk. Since E_{bulk} is the same before and after Li/Ni mixing, the difference in the surface energy $\Delta\gamma$ is equal to the formation energy of Li/Ni mixing:

$$\Delta\gamma = \gamma^{Li/Ni} - \gamma^{pristine} = \Delta E_{formation}. \quad (11)$$

The formation energy of the substitutional dopant can be calculated using

$$\Delta E_{formation}^{i} = E_{slab}^{i} + n_j\mu_j - E_{slab} - n_i\mu_i + qE_F, \quad (12)$$

where superscript i represents the dopants (Co, Mn, F, and S), and superscript j represents the replaced atoms (Ni and O); n_i is the number of the dopant atoms; and n_i is the number of the replaced atoms. The chemical potentials of elements O and F can be estimated from F_2 and O_2 gas. For example, $\mu_O = \mu_{O_2}/2$. The chemical potentials of elements S, Ni, Co, and Mn can be estimated in the most common solid forms. The space groups of elementary substance sulfur, nickel, manganese, and cobalt are *Fdddz*, $Fm\bar{3}m$, $I\bar{4}3m$, and $P6_3/mmc$, respectively. We denote by q the difference in charge state at the doping sites and by E_F the Fermi energy. Since there is no band gap in both the bulk and the (110) surface of $LiNiO_2$, we do not consider the Coulomb interaction term (the last term) in the formation energy.

ACKNOWLEDGMENTS

This work is supported by the National Natural Science Foundation of China (Grants No. 52272180, No. 12174162, No. 51962010), the Fujian Science & Technology Innovation Laboratory for Energy Devices of China (21C-LAB), and IER Foundation 2021 (IERF202104).

The authors declare no conflict of interest.

[1] F. Schipper, E. M. Erickson, C. Erk, J.-Y. Shin, F. F. Chesneau, and D. Aurbach, Review—Recent advances and remaining challenges for lithium ion battery cathodes, J. Electrochem. Soc. **164**, A6220 (2016).

[2] S.-T. Myung, F. Maglia, K.-J. Park, C. S. Yoon, P. Lamp, S.-J. Kim, and Y.-K. Sun, Nickel-rich layered cathode materials for automotive lithium-ion batteries: Achievements and perspectives, ACS Energy Lett. **2**, 196 (2017).

[3] R. Schmuch, R. Wagner, G. Hörpel, T. Placke, and M. Winter, Performance and cost of materials for lithium-based rechargeable automotive batteries, Nat. Energy **3**, 267 (2018).

[4] A. Chen, K. Wang, J. Li, Q. Mao, Z. Xiao, D. Zhu, G. Wang, P. Liao, J. He, Y. You, and Y. Xia, The formation, detriment and solution of residual lithium compounds on Ni-rich layered oxides in lithium-ion batteries, Front. Energy Res. **8**, 593009 (2020).

[5] H.-J. Noh, S. Youn, C. S. Yoon, and Y.-K. Sun, Comparison of the structural and electrochemical properties of layered $LiNi_xCo_yMn_zO_2$ ($x = 1/3$, 0.5, 0.6, 0.7, 0.8 and 0.85) cathode material for lithium-ion batteries, J. Power Sources **233**, 121 (2013).

[6] C. Liang, R. C. Longo, F. Kong, C. Zhang, Y. Nie, Y. Zheng, and K. Cho, Ab initio study on surface segregation and anisotropy of Ni-rich $LiNi_{1-2y}Co_yMn_yO_2$ (NCM) ($y \leq 0.1$) cathodes, ACS Appl. Mater. Interfaces **10**, 6673 (2018).

[7] C. Liang, F. Kong, R. C. Longo, S. KC, J.-S. Kim, S. Jeon, S. Choi, and K. Cho, Unraveling the origin of instability in Ni-rich $LiNi_{1-2x}Co_xMn_xO_2$ (NCM) cathode materials, J. Phys. Chem. C **120**, 6383 (2016).

[8] H. Liu, Y. Yang, and J. Zhang, Investigation and improvement on the storage property of $LiNi_{0.8}Co_{0.2}O_2$ as a cathode material for lithium-ion batteries, J. Power Sources **162**, 644 (2006).

[9] Y. You, H. Celio, J. Li, A. Dolocan, and A. Manthiram, Modified high-nickel cathodes with stable surface chemistry against ambient air for lithium-ion batteries, Angew. Chem., Int. Ed. **57**, 6480 (2018).

[10] Y. Saito, M. Shikano, and H. Kobayashi, State of charge (SOC) dependence of lithium carbonate on $LiNi_{0.8}Co_{0.15}Al_{0.05}O_2$ electrode for lithium-ion batteries, J. Power Sources **196**, 6889 (2011).

[11] D.-H. Cho, C.-H. Jo, W. Cho, Y.-J. Kim, H. Yashiro, Y.-K. Sun, and S.-T. Myung, Effect of residual lithium compounds on layer Ni-rich $LiNi_{0.7}Mn_{0.3}O_2$, J. Electrochem. Soc. **161**, A920 (2014).

[12] C. Busà, M. Belekoukia, and M. J. Loveridge, The effects of ambient storage conditions on the structural and electrochemical properties of NMC-811 cathodes for Li-ion batteries, Electrochim. Acta **366**, 137358 (2021).

[13] S. Hwang, W. Chang, S. M. Kim, D. Su, D. H. Kim, J. Y. Lee, K. Y. Chung, and E. A. Stach, Investigation of changes

in the surface structure of $Li_xNi_{0.8}Co_{0.15}Al_{0.05}O_2$ cathode materials induced by the initial charge, Chem. Mater. **26**, 1084 (2014).

[14] C.-K. Lin, Y. Ren, K. Amine, Y. Qin, and Z. Chen, In situ high-energy x-ray diffraction to study overcharge abuse of 18650-size lithium-ion battery, J. Power Sources **230**, 32 (2013).

[15] J. Vetter, P. Novák, M. Wagner, C. Veit, K.-C. Möller, J. Besenhard, M. Winter, M. Wohlfahrt-Mehrens, C. Vogler, and A. Hammouche, Ageing mechanisms in lithium-ion batteries, J. Power Sources **147**, 269 (2005).

[16] Y. Kim, Mechanism of gas evolution from the cathode of lithium-ion batteries at the initial stage of high-temperature storage, J. Mater. Sci. **48**, 8547 (2013).

[17] R. Jung, P. Strobl, F. Maglia, C. Stinner, and H. A. Gasteiger, Temperature dependence of oxygen release from $LiNi_{0.6}Mn_{0.2}Co_{0.2}O_2$ (NMC622) cathode materials for Li-ion batteries, J. Electrochem. Soc. **165**, A2869 (2018).

[18] P. Hou, J. Yin, M. Ding, J. Huang, and X. Xu, Surface/interfacial structure and chemistry of high-energy nickel-rich layered oxide cathodes: Advances and perspectives, Small **13**, 1701802 (2017).

[19] L. Liang, W. Zhang, F. Zhao, D. K. Denis, F. u. Zaman, L. Hou, and C. Yuan, Surface/interface structure degradation of Ni-rich layered oxide cathodes toward lithium-ion batteries: Fundamental mechanisms and remedying strategies, Adv. Mater. Interfaces **7**, 1901749 (2020).

[20] N. Y. Kim, T. Yim, J. H. Song, J.-S. Yu, and Z. Lee, Microstructural study on degradation mechanism of layered $LiNi_{0.6}Co_{0.2}Mn_{0.2}O_2$ cathode materials by analytical transmission electron microscopy, J. Power Sources **307**, 641 (2016).

[21] K. Kleiner, J. Melke, M. Merz, P. Jakes, P. Nagel, S. Schuppler, V. Liebau, and H. Ehrenberg, Unraveling the degradation process of $LiNi_{0.8}Co_{0.15}Al_{0.05}O_2$ electrodes in commercial lithium ion batteries by electronic structure investigations, ACS Appl. Mater. Interfaces **7**, 19589 (2015).

[22] W. M. Seong, Y. Kim, and A. Manthiram, Impact of residual lithium on the adoption of high-nickel layered oxide cathodes for lithium-ion batteries, Chem. Mater. **32**, 9479 (2020).

[23] J. Marchand-Brynaert, N. Jongen, and J.-L. Dewez, Surface hydroxylation of poly(vinylidene fluoride) (PVDF) film, J. Polym. Sci., Part A: Polym. Chem. **35**, 1227 (1997).

[24] G. Ross, J. Watts, M. Hill, and P. Morrissey, Surface modification of poly(vinylidene fluoride) by alkaline treatment Part 2. Process modification by the use of phase transfer catalysts, Polymer **42**, 403 (2001).

[25] J. Eom, M. G. Kim, and J. Cho, Storage characteristics of $LiNi_{0.8}Co_{0.1+x}Mn_{0.1-x}O_2$ ($x = 0, 0.03$, and 0.06) cathode materials for lithium batteries, J. Electrochem. Soc. **155**, A239 (2008).

[26] B. Han, S. Xu, S. Zhao, G. Lin, Y. Feng, L. Chen, D. G. Ivey, P. Wang, and W. Wei, Enhancing the structural stability of Ni-rich layered oxide cathodes with a preformed Zr-concentrated defective nanolayer, ACS Appl. Mater. Interfaces **10**, 39599 (2018).

[27] Y. Lai, J. Wu, Y. Tang, G. Shang, X. Yang, H. Fan, C. Peng, and Z. Zhang, Alleviating the air sensitivity of nickel-rich $LiNi_{0.815}Co_{0.15}Al_{0.035}O_2$ cathode by Zr^{4+}-modification for Li-ion batteries, Ceram. Int. **45**, 14270 (2019).

[28] B. Huang, D. Liu, K. Qian, L. Zhang, K. Zhou, Y. Liu, F. Kang, and B. Li, A simple method for the complete performance recovery of degraded Ni-rich $LiNi_{0.70}Co_{0.15}Mn_{0.15}O_2$ cathode via surface reconstruction, ACS Appl. Mater. Interfaces **11**, 14076 (2019).

[29] K. Park, J.-H. Park, S.-G. Hong, B. Choi, S. Heo, S.-W. Seo, K. Min, and J.-H. Park, Re-construction layer effect of $LiNi_{0.8}Co_{0.15}Mn_{0.05}O_2$ with solvent evaporation process, Sci. Rep. **7**, 1 (2017).

[30] J. Kim, H. Lee, H. Cha, M. Yoon, M. Park, and J. Cho, Prospect and reality of Ni-rich cathode for commercialization, Adv. Energy Mater. **8**, 1702028 (2018).

[31] X. Xiong, Z. Wang, P. Yue, H. Guo, F. Wu, J. Wang, and X. Li, Washing effects on electrochemical performance and storage characteristics of $LiNi_{0.8}Co_{0.1}Mn_{0.1}O_2$ as cathode material for lithium-ion batteries, J. Power Sources **222**, 318 (2013).

[32] X. Zheng, X. Li, Z. Wang, H. Guo, Z. Huang, G. Yan, and D. Wang, Investigation and improvement on the electrochemical performance and storage characteristics of $LiNiO_2$-based materials for lithium ion battery, Electrochim. Acta **191**, 832 (2016).

[33] J. Cho, T.-J. Kim, J. Kim, M. Noh, and B. Park, Synthesis, thermal, and electrochemical properties of $AlPO_4^-$ coated $LiNi_{0.8}Co_{0.1}Mn_{0.1}O_2$ cathode materials for a Li-ion cell, J. Electrochem. Soc. **151**, A1899 (2004).

[34] Y. Kim and J. Cho, Lithium-reactive $Co_3(PO_4)_2$ nanoparticle coating on high-capacity $LiNi_{0.8}Co_{0.16}Al_{0.04}O_2$ cathode material for lithium rechargeable batteries, J. Electrochem. Soc. **154**, A495 (2007).

[35] C.-H. Jo, D.-H. Cho, H.-J. Noh, H. Yashiro, Y.-K. Sun, and S. T. Myung, An effective method to reduce residual lithium compounds on Ni-rich $LiNi_{0.6}Co_{0.2}Mn_{0.2}O_2$ active material using a phosphoric acid derived Li_3PO_4 nanolayer, Nano Res. **8**, 1464 (2015).

[36] M.-J. Lee, M. Noh, M.-H. Park, M. Jo, H. Kim, H. Nam, and J. Cho, The role of nanoscale-range vanadium treatment in $LiNi_{0.8}Co_{0.15}Al_{0.05}O_2$ cathode materials for Li-ion batteries at elevated temperatures, J. Mater. Chem. A **3**, 13453 (2015).

[37] J.-L. Shi, R. Qi, X.-D. Zhang, P.-F. Wang, W.-G. Fu, Y.-X. Yin, J. Xu, L.-J. Wan, and Y.-G. Guo, High-thermal- and air-stability cathode material with concentration-gradient buffer for Li-ion batteries, ACS Appl. Mater. Interfaces **9**, 42829 (2017).

[38] J. Zhang, Z. Yang, R. Gao, L. Gu, Z. Hu, and X. Liu, Suppressing the structure deterioration of Ni-rich $LiNi_{0.8}Co_{0.1}Mn_{0.1}O_2$ through atom-scale interfacial integration of self-forming hierarchical spinel layer with Ni gradient concentration, ACS Appl. Mater. Interfaces **9**, 29794 (2017).

[39] Y.-K. Sun, S.-T. Myung, M.-H. Kim, J. Prakash, and K. Amine, Synthesis and characterization of $Li(Ni_{0.8}Co_{0.1}Mn_{0.1})_{0.8}(Ni_{0.5}Mn_{0.5})_{0.2}O_2$ with the microscale core-shell structure as the positive electrode material for lithium batteries, J. Am. Chem. Soc. **127**, 13411 (2005).

[40] B.-B. Lim, S.-T. Myung, C. S. Yoon, and Y.-K. Sun, Comparative study of Ni-rich layered cathodes for

rechargeable lithium batteries: $LiNi_{0.85}Co_{0.11}Al_{0.04}O_2$ and $LiNi_{0.84}Co_{0.06}Mn_{0.09}Al_{0.01}O_2$ with two-step full concentration gradients, ACS Energy Lett. **1**, 283 (2016).

[41] Y. Kim, Water adsorption on the surface of Ni- and Co-based layer-structured cathode materials for lithium-ion batteries, Int. J. Quantum Chem. **118**, e25591 (2018).

[42] Z. Fang, M. P. Confer, Y. Wang, Q. Wang, M. R. Kunz, E. J. Dufek, B. Liaw, T. M. Klein, D. A. Dixon, and R. Fushimi, Formation of surface impurities on lithium-nickel-manganese-cobalt oxides in the presence of CO_2 and H_2O, J. Am. Chem. Soc. **143**, 10261 (2021).

[43] J. Jiao, G. Lai, S. Qin, C. Fang, X. Xu, Y. Jiang, C. Ouyang, and J. Zheng, Tuning of surface morphology in Li layered oxide cathode materials, Acta Mater. **238**, 118229 (2022).

[44] T. Ohzuku, A. Ueda, M. Nagayama, Y. Iwakoshi, and H. Komori, Comparative study of $LiCoO_2$, $LiNi_{12}Co_{12}O_2$ and $LiNiO_2$ for 4 volt secondary lithium cells, Electrochim. Acta **38**, 1159 (1993).

[45] H. Arai, S. Okada, H. Ohtsuka, M. Ichimura, and J. Yamaki, Characterization and cathode performance of $Li_{1-x}Ni_{1+x}O_2$ prepared with the excess lithium method, Solid State Ionics **80**, 261 (1995).

[46] T. Nohma, H. Kurokawa, M. Uehara, M. Takahashi, K. Nishio, and T. Saito, Electrochemical characteristics of $LiNiO_2$ and $LiCoO_2$ as a positive material for lithium secondary batteries, J. Power Sources **54**, 522 (1995).

[47] D. Aurbach, Y. Ein-Eli, B. Markovsky, A. Zaban, S. Luski, Y. Carmeli, and H. Yamin, The study of electrolyte solutions based on ethylene and diethyl carbonates for rechargeable Li batteries: II. Graphite electrodes, J. Electrochem. Soc. **142**, 2882 (1995).

[48] T. Toma, R. Maezono, and K. Hongo, Electrochemical properties and crystal structure of Li^+/H^+ cation-exchanged $LiNiO_2$, ACS Appl. Energy Mater. **3**, 4078 (2020).

[49] I. A. Shkrob, J. A. Gilbert, P. J. Phillips, R. Klie, R. T. Haasch, J. Bareño, and D. P. Abraham, Chemical weathering of layered Ni-rich oxide electrode materials: Evidence for cation exchange, J. Electrochem. Soc. **164**, A1489 (2017).

[50] M. Hofmann, M. Kapuschinski, U. Guntow, and G. A. Giffin, Implications of aqueous processing for high energy density cathode materials: Part II. Water-induced surface species on $LiNi_{0.8}Co_{0.15}Al_{0.05}O_2$, J. Electrochem. Soc. **167**, 140535 (2020).

[51] K. Shizuka, C. Kiyohara, K. Shima, and Y. Takeda, Effect of CO_2 on layered $Li_{1+z}Ni_{1-x-y}Co_xM_yO_2$ (M = Al, Mn) cathode materials for lithium ion batteries, J. Power Sources **166**, 233 (2007).

[52] H. Liu, Y. Yang, and J. Zhang, Reaction mechanism and kinetics of lithium ion battery cathode material $LiNiO_2$ with CO_2, J. Power Sources **173**, 556 (2007).

[53] K. Matsumoto, R. Kuzuo, K. Takeya, and A. Yamanaka, Effects of CO_2 in air on Li deintercalation from $LiNi_{1-x-y}Co_xAl_yO_2$, J. Power Sources **81**, 558 (1999).

[54] N. V. Faenza, L. Bruce, Z. W. Lebens-Higgins, I. Plitz, N. Pereira, L. F. J. Piper, and G. G. Amatucci, Editors' choice—Growth of ambient induced surface impurity species on layered positive electrode materials and impact on electrochemical performance, J. Electrochem. Soc. **164**, A3727 (2017).

[55] See Supplemental Material at http://link.aps.org/supplemental/10.1103/PRXEnergy.2.033001, which includes Refs. [43,70,83,84,86], for details of the model construction, PDOS analysis, structural relaxation calculation results, and discussion of the Jahn-Teller distortion effects on air sensitivity.

[56] M.-F. Lin, N. Singh, S. Liang, M. Mo, J. P. F. Nunes, K. Ledbetter, J. Yang, M. Kozina, S. Weathersby, X. Shen, A. A. Cordones, T. J. A. Wolf, C. D. Pemmaraju, M. Ihme, and X. J. Wang, Imaging the short-lived hydroxyl-hydronium pair in ionized liquid water, Science **374**, 92 (2021).

[57] E. Cho, S.-W. Seo, and K. Min, Theoretical prediction of surface stability and morphology of $LiNiO_2$ cathode for Li ion batteries, ACS Appl. Mater. Interfaces **9**, 33257 (2017).

[58] S.-U. Woo, B.-C. Park, C. S. Yoon, S.-T. Myung, J. Prakash, and Y.-K. Sun, Improvement of electrochemical performances of $LiNi_{0.8}Co_{0.1}Mn_{0.1}O_2$ cathode materials by fluorine substitution, J. Electrochem. Soc. **154**, A649 (2007).

[59] S. H. Park, Y.-K. Sun, K. S. Park, K. S. Nahm, Y. S. Lee, and M. Yoshio, Synthesis and electrochemical properties of lithium nickel oxysulfide ($LiNiS_yO_{2-y}$) material for lithium secondary batteries, Electrochim. Acta **47**, 1721 (2002).

[60] G. Kresse and J. Furthmüller, Efficiency of ab-initio total energy calculations for metals and semiconductors using a plane-wave basis set, Comput. Mater. Sci. **6**, 15 (1996).

[61] G. Kresse and J. Furthmüller, Efficient iterative schemes for ab initio total-energy calculations using a plane-wave basis set, Phys. Rev. B **54**, 11169 (1996).

[62] P. E. Blöchl, Projector augmented-wave method, Phys. Rev. B **50**, 17953 (1994).

[63] J. P. Perdew, K. Burke, and M. Ernzerhof, Generalized Gradient Approximation Made Simple, Phys. Rev. Lett. **77**, 3865 (1996).

[64] S. Grimme, J. Antony, S. Ehrlich, and H. Krieg, A consistent and accurate ab initio parametrization of density functional dispersion correction (DFT-D) for the 94 elements H-Pu, J. Chem. Phys. **132**, 154104 (2010).

[65] B. Himmetoglu, A. Floris, S. de Gironcoli, and M. Cococcioni, Hubbard-corrected DFT energy functionals: The LDA+U description of correlated systems, Int. J. Quantum Chem. **114**, 14 (2014).

[66] J. Cheng, L. Mu, C. Wang, Z. Yang, H. L. Xin, F. Lin, and K. A. Persson, Enhancing surface oxygen retention through theory-guided doping selection in $Li_{1-x}NiO_2$ for next-generation lithium-ion batteries, J. Mater. Chem. A **8**, 23293 (2020).

[67] D. Kramer and G. Ceder, Tailoring the morphology of $LiCoO_2$: A first principles study, Chem. Mater. **21**, 3799 (2009).

[68] L. Wang, T. Maxisch, and G. Ceder, Oxidation energies of transition metal oxides within the GGA+U framework, Phys. Rev. B **73**, 195107 (2006).

[69] J. Heyd, G. E. Scuseria, and M. Ernzerhof, Hybrid functionals based on a screened Coulomb potential, J. Chem. Phys. **118**, 8207 (2003).

[70] W. Jia, Z. Cao, L. Wang, J. Fu, X. Chi, W. Gao, and L.-W. Wang, The analysis of a plane wave pseudopotential density functional theory code on a GPU machine, Comput. Phys. Commun. **184**, 9 (2013).

[71] P. Xiao, D. Sheppard, J. Rogal, and G. Henkelman, Solid-state dimer method for calculating solid-solid phase transitions, J. Chem. Phys. **140**, 174104 (2014).

[72] J. Kästner and P. Sherwood, Superlinearly converging dimer method for transition state search, J. Chem. Phys. **128**, 014106 (2008).

[73] A. Heyden, A. T. Bell, and F. J. Keil, Efficient methods for finding transition states in chemical reactions: Comparison of improved dimer method and partitioned rational function optimization method, J. Chem. Phys. **123**, 224101 (2005).

[74] G. Henkelman and H. Jónsson, A dimer method for finding saddle points on high dimensional potential surfaces using only first derivatives, J. Chem. Phys. **111**, 7010 (1999).

[75] R. Dronskowski and P. E. Bloechl, Crystal orbital Hamilton populations (COHP): Energy-resolved visualization of chemical bonding in solids based on density-functional calculations, J. Phys. Chem. **97**, 8617 (1993).

[76] V. L. Deringer, A. L. Tchougréeff, and R. Dronskowski, Crystal orbital Hamilton population (COHP) analysis as projected from plane-wave basis sets, J. Phys. Chem. A **115**, 5461 (2011).

[77] S. Maintz, V. L. Deringer, A. L. Tchougréeff, and R. Dronskowski, Analytic projection from plane-wave and PAW wavefunctions and application to chemical-bonding analysis in solids, J. Comput. Chem. **34**, 2557 (2013).

[78] S. Maintz, V. L. Deringer, A. L. Tchougréeff, and R. Dronskowski, LOBSTER: A tool to extract chemical bonding from plane-wave based DFT.J. Comput. Chem. **37**,1030 (2016).

[79] S. Maintz, M. Esser, and R. Dronskowski, Efficient rotation of local basis functions using real spherical harmonics, Acta Phys. Pol. B **47**,1165 (2016).

[80] R. Nelson, C. Ertural, J. George, V. L. Deringer, G. Hautier, and R. Dronskowski, LOBSTER: Local orbital projections, atomic charges, and chemical-bonding analysis from projector-augmented-wave-based density-functional theory, J. Comput. Chem. **41**, 1931 (2020).

[81] K. Momma and F. Izumi, VESTA 3 for three-dimensional visualization of crystal, volumetric and morphology data, J. Appl. Crystallogr. **44**, 1272 (2011).

[82] A. Stukowski, Visualization and analysis of atomistic simulation data with OVITO—the open visualization tool, Model. Simul. Mat. Sci. Eng. **18**, 015012 (2009).

[83] P. Kalyani and N. Kalaiselvi, Various aspects of $LiNiO_2$ chemistry: A review, Sci. Technol. Adv. Mater. **6**, 689 (2005).

[84] M. Bianchini, M. Roca-Ayats, P. Hartmann, T. Brezesinski, and J. Janek, There and back again—The journey of $LiNiO_2$ as a cathode active material, Angew. Chem. Int. Ed. **58**, 10434 (2019).

[85] J. Zhu and G. Chen, Single-crystal based studies for correlating the properties and high-voltage performance of $LiNi_xMn_yCo_{1-x-y}O_2$ cathodes, J. Mater. Chem. A **7**, 5463 (2019).

[86] Y. Kim, H. Lee, and S. Kang, First-principles and experimental investigation of the morphology of layer-structured $LiNiO_2$ and $LiCoO_2$, J. Mater. Chem. **22**, 12874 (2012).

[87] Z. Wang, H. Liu, J. Wu, W.-M. Lau, J. Mei, H. Liu, and G. Liu, Hierarchical $LiNi_{0.8}Co_{0.15}Al_{0.05}O_2$ plates with exposed {010} active planes as a high performance cathode material for Li-ion batteries, RSC Adv. **6**, 32365 (2016).

[88] F. Li, Z. Liu, J. Shen, X. Xu, L. Zeng, Y. Li, D. Zhang, S. Zuo, and J. Liu, Ni-rich layered oxide with preferred orientation (110) plane as a stable cathode material for high-energy lithium-ion batteries, Nanomaterials **10**, 2495 (2020).

[89] S. Zhou, T. Mei, X. Wang, and Y. Qian, Crystal structural design of exposed planes: Express channels, high-rate capability cathodes for lithium-ion batteries, Nanoscale **10**, 17435 (2018).

[90] W. Xiang, W.-Y. Liu, J. Zhang, S. Wang, T.-T. Zhang, K. Yin, X. Peng, Y.-C. Jiang, K.-H. Liu, and X.-D. Guo, Controlled synthesis of nickel-rich layered oxide cathodes with preferentially exposed {010} active facets for high rate and long cycling stable lithium-ion batteries, J. Alloys Compd. **775**, 72 (2019).